POLITECNICO DI TORINO
Repository ISTITUZIONALE

Pore structure characterization through path-finding
and Lattice Boltzmann simulation

(Article begins on next page)

30 April 2024

Pore structure characterization through path-finding and Lattice Boltzmann simulation

Dario Viberti, Costanzo Peter, Eloisa Salina Borello, Filippo Panini*

Department of Environment, Land and Infrastructure Engineering, Politecnico di Torino, Turin 1024, Italy

Abstract

Characterization of underground porous media parameters at the micro and macro scales is fundamental in geosciences. A thorough comprehension of flow phenomena requires analyses and observations at the micro scale through adoption of micromodels as much as possible representative of real geological formations. In this paper we focus on the analysis of 2D binary images of real rock thin sections to characterize pore network geometry and to estimate effective porosity, pore size distribution and tortuosity with the aim of providing suitable information for designing micromodels. To this end, a geometrical analysis of the pore structure, based on the identification and characterization of the set of shortest geometrical pathways between inlets and outlets pairs, was implemented. The geometrical analysis is based on a path-finding algorithm derived from graph theory. Results provided by geometrical analysis were validated against hydrodynamic numerical simulation via the Lattice Boltzmann Method (LBM). Results show that the path-finding approach provides reasonable and reliable estimates of tortuosity and can be successfully applied for analyzing the distribution of effective pore radius, as well as for estimating the effective porosity.

Keywords: pore structure, tortuosity, Lattice Boltzmann Method, path-finding algorithm, effective porosity

1. Introduction

The characterization of fluid flow in underground porous media at the micro and macro scales is crucial in several areas such as in groundwater, environmental and reservoir engineering and geosciences. Laboratory analyses on rock cores provide fundamental macroscale parameters such as porosity, absolute and relative permeability and capillary pressure curves. However, a thorough comprehension of single and multiphase flow phenomena requires analyses

---

*Corresponding author
  Email address: `filippo.panini@polito.it` (Filippo Panini)

and observations at the micro scale [1, 2]. In this view, a great opportunity is given by observation of flow phenomena in microfluidic devices designed as physical micromodels representing pseudo two-dimensional capillary networks [3]. Multi-scale studies associated with pore network properties are increasingly used to improve understanding of behavior features and multiphase flow properties in porous media at the phenomenological scale [4]. These include distribution of pores space (micropore/macropore), connectivity, constricted porosity by throats, hysteresis, fluid occupancy during multiphase or displacement processes, wettability [4]. Pore network rules liquid and gas permeability properties, as well as water retention, and electro-chemical transport [4]. Real geological formation are often characterized by high degree of heterogeneities and complexity of the pore network geometry that should be taken into account in the design of the micromodels [5].

In the current paper we explore the possibility of adopting a path-finding algorithm for characterization of pore structure, geometry and connectivity with the aim of analyzing 2D binary images of rock samples representative or real geological formations and providing geometrical parameters that could be used, in future works, to design microfluidic devices. The path-finding algorithm has been applied to several real rock images and results are validated through the application of simple 2D LBM simulation.

The lattice Boltzmann method (LBM) is well suited for simulating fluid flow at the pore-scale in complex geometries. Several authors used it to study the fluid flow at pore scale of micromodels, synthetic porous media or real rock samples. Venturoli and Boek [3] and Laleian et al. [6] used 2D LBM with single relaxation time (SRT) to calculate the fluid flow in micromodels taking the third dimension into account by adding a drag force. Boek and Venturoli [7] used the same approach for studying the fluid flow in a quasi-two-dimensional micromodel based on the image of a Berea sandstone. Wu et al. [5] compared single and multiphase flow by LBM simulation of a micromodel with results obtained by laboratory experiments. Koponen et al. used the LGA method to estimate permeability, effective porosity ([8]) and tortuosity ([9]) in synthetic 2D porous media. Ghassemi and Park [10] used LBM to study the effects of permeability and tortuosity on flow through 2D saturated particulate media and Li et al. [11] studied the effect of geometrical properties on saturation and relative permeability in 2D synthetic porous media. Yang et al.[12] used 3D LBM for permeability assessment in random packed porous media. Comparison of single and multiple relaxation time (MRT) LBM for permeability assessment was performed in 2D synthetic porous media (Pan et al. [13]) and 3D synthetic and real porous media (Eshghinejadfard et al. [14]). Ferreol et al. [15] with LBM simulated single-phase and two-phase flow through three-dimensional tomographic reconstructions of Fontainebleau sandstone. Xu et al. [16] used LBM to investigate relative permeability and specific interfacial length by simulating immiscible two-phase flow in 2D sample of Berea sandstone.

Porous media are complex materials characterized by a chaotic structure and tortuous fluid flow, with pore and grains dimension varying over a wide range [17]. To address the crooked fluid paths of pore structure, the concept of tortu-

osity (τ) was introduced [18]. Basically, two main types of tortuosity are defined in the literature: geometrical tortuosity (τ_g) and hydraulic tortuosity (τ_h). Geometrical tortuosity is defined as the shortest length between inflow and outflow points that avoids the solid obstacles divided by the distance between inlet and outlet [19, 20]. Hydraulic tortuosity is defined as the effective path length taken by the fluid divided by the length of the porous material measured on the flow direction [18]. Since, the fluid flow path is always greater than the shortest geometrical path, hydraulic tortuosity is always greater than the geometrical tortuosity [20, 17]. For a complete review on the definitions of tortuosity, the reader can refer to [20] and to [17].

To account for pore space interconnections affected by the flow, the effective porosity (ϕ_e) was introduced; it is defined as the percentage of conductive pore space with respect to the bulk volume [21, 8]:

$$\phi_e = \frac{V_{flow}}{V_b} \tag{1}$$

where V_{flow} is the portion of volume contributing to the fluid flow.

The impact of pore network geometry on flow behavior is well recognized.In the literature, several analytic expressions have been provided [9, 22, 23, 18, 24] to link permeability to the pore structure as a function of porosity, effective porosity, tortuosity and/or pore dimension and hydraulic radius (r_H), which gives a measure of the average pore dimension [25, 26].

Several authors discussed the geometrical analysis of the pore structure from 2D and 3D images. Comparison of three image processing algorithms (Mean Intercept Length, Erosion and Dilation, Watershed Segmentation) to estimate the grain-size distribution of porous rocks from binary 2D images has been performed by Rabbani et al. [27]. Lock et al. [28] developed a network model that allows predictions of the permeability of consolidated sedimentary rocks, based on image analysis of sections of a rock core sample. Lindquist et al. [29] discuss the medial axes method to analyze structure properties such as pore throat and pore body size distributions and geometric tortuosity of a 3D digitalized image. Later, Sun et al. [30] used a shortest past approach based on Dijkstra's algorithm to calculate the geometric tortuosity and connected porosity; then, they applied a multiscale method approach to upscale the permeability. Ju et al. [31] proposed an algorithm to predict preferential flow paths based on the topologically equivalent network of a porous structure and the flow resistance of flow paths and Keller et al. [32] a 3D graph representation to determine the spatial distribution of pore space geometrical properties. In [17, 33, 34], the authors proposed geometric tortuosity models based on concepts from finite-size scaling analysis and percolation theory. Al-Raoush and Madhoun [35] presented an algorithm for calculating geometric tortuosity from 3D X-ray tomography images of real rocks based on a guided search for connected paths utilizing the medial surface of the void space of a 3D segmented image.

In this paper we focus on methods to estimate, from 2D binary images of a rock sample, parameters which allows to describe the pore structure. To this aim we applied an approach based on geometrical analysis of the porous media.

3

The geometrical approach was developed based on a A* path-finding procedure taken from the graph theory. This approach was validated for the parameters of interest of the study with the more established hydrodynamic based path analysis carried out by numerical simulation via the Lattice Boltzmann Method (LBM). A preliminary validation of the methodologies was carried out on a set of simplified synthetic cases for which the true value of the parameters of interest was analytically computed. Successively, the methodologies were applied to images of real rock sample thin sections taken from literature.

2. Material and methods

Starting point for the presented methodologies is a 2D binary image of a rock section. Such data can be obtained by image processing of the Scanning Electron Microscopy (SEM) image of a thin section or the slice of an X-ray micro-tomography image. Preliminary image processing is beyond the scope of this paper, however readers interested on the topic may consult [36, 37, 38]. In this paper we analyzed a set of literature images obtained from thin sections of 3D samples of sedimentary rocks; when necessary, a preliminary image processing was applied to convert gray scale images to binary files (see section 4). On the 2D binary image we analyzed the pore structure in terms of pathways accessible by fluid flow in monophase conditions and calculated the associated parameters: tortuosity (Sections 2.3.2 and 2.3.3) and effective porosity (Section 2.3.4). Two different approaches were applied to assess pathways: geometrical (Section 2.1) and hydrodynamic (Section 2.2). The pore structure analysis was completed by calculation of pore radius variations along the path (Section 2.3.1) compared with the hydraulic radius, which represents the pore radius of an equivalent capillary tube (see Eq. 4).

2.1. Geometrical path calculation

The pore structure of a binary 2D image is analyzed through a path-finding method based on graph representation. To this end, a set of inlets n_{in} and outlets n_{out} are placed along the inner and outer boundaries of the image of the porous domain orthogonal to the main flow direction (x or y); the centroids of the pixels are used as reference grid node locations. These locations represent the points where the fluid enters and potentially leaves the porous system respectively.

The shortest pathway between each couple of inlet-outlet points is obtained through the path-finding method A* algorithm [39, 40, 41]. A* is based on a cost function $f(n)$ to determine the optimal path between two nodes:

$$f(n) = g(n) + h(n) \tag{2}$$

where n indicates the considered node, $g(n)$ the incremental distance from the considered node to the initial node and $h(n)$ is a heuristic function used to obtain a prior estimation to reach the target from the considered node.

4

The process of obtaining the optimal shortest path is achieved by steps. Starting at the initial node, the cost function $f(n)$ is calculated at each adjacent nodes in order to identify the one having the minimum cost which will be used as reference for the next calculation. This process is progressively repeated until the target is reached. The output is represented as a graph $G = (N, E)$ with N being a set of nodes with $X - Y$ coordinates while E the edges connecting the nodes (Fig. 1).

The application of A* algorithm to the images gives a set of $n_{in} \times n_{out}$ coordinates of the shortest paths in a fixed direction, whose length L_{sh} can be easily calculated by applying the euclidean distance.

2.2. Hydraulic path calculation

Hydraulic paths were obtained as a result of numerical simulation of monophase fluid flow at the pore-scale. To this end, we implemented a discrete mesoscopic computational methods based on the Lattice Boltzmann Method (LBM). The LBM is a relatively new computational fluid dynamics (CFD) method, first appeared in the 1980s [42], successively developed by several authors [43] and still subject of research activity. The LBM has shown to be a functional technique for the computational modeling of a wide variety of complex fluid flow problems including single and multiphase flows in complex geometries ([44, 45, 7]) and porous media [46]. Use of the LBM to evaluate the hydraulic tortuosity in synthetic porous media was presented by [47, 48, 49].
The implementation adopted in this paper for mono-phase flow simulation in porous media is based on a single-relaxation time (SRT) approximation of the collision operator, called the Bhatnagar-Gross-Krook model (BGK) [50]. The relaxation time was set equal to 1 and the time step was calculated in accordingly to guarantee stability conditions [43].The nine-velocity square lattice model D2Q9 [51] was adopted to discretize the domain. At the fluid-solid interface, no-slip condition was imposed via halfway bounce-back [52]. Fixed pressure gradient between inlet and outlet was assumed as the boundary condition, which was implemented via non-equilibrium bounce-back [53]. No-flow boundaries parallel to the main flow direction were assumed to reproduce laboratory conditions; they were implemented with halfway bounce-back [52].

2.3. Characterization of pore structure

A quantitative microstructure characterization of the porous medium is carried out through the estimation of a series of parameters: pore size(Section 2.3.1), tortuosity (geometrical, Section 2.3.2, and hydraulic, Section 2.3.3) and effective porosity (Section 2.3.4). In the following we will not parametrize pore structure in terms of pore throat and pore body; we will refer to the local aperture between the pore walls as pore size or to the semi-aperture as pore radius.

2.3.1. Pore size

Along the geometrical pathways identified by A* algorithm, the pore size is calculated at each node location by measuring the extension of the pore section length orthogonal to the local path direction (Fig. 1).
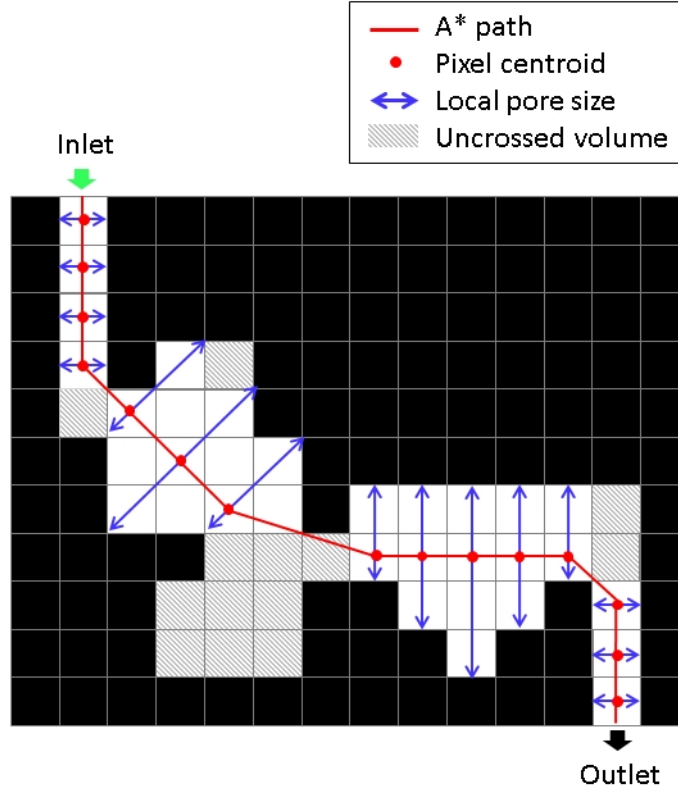
Figure 1: Schematic of pore sizeand effective porosity estimation from path-finding approach.

The local pore size estimation allows to monitor the pore radius (r_p) evolution along each detected path. This information can be used for reconstructing 3D porous geometries ([54, 55]) or for comparative analysis with hydrodynamic data.

The output is also analyzed by a statistical representation of the pore radius distribution of the sample, which is compared with the hydraulic radius (r_H), defined as [26]:

$$r_H = \phi_{3D} \frac{V_b}{A_w} \tag{3}$$

where V_b is the bulk volume of the system (pore and grain) and A_w is the wetted surface, i.e. the surface area between grain and void. Transposing it to a 2D

6

section, it becomes:

$$r_H = \phi \frac{A_b}{P_w} \qquad (4)$$

where A_b is the bulk area of the sample and P_w is the wetted perimeter, i.e. the interface between grains and void, which can be easily calculated by image processing routine; we used the Image Processing Toolbox of MATLAB [56]. The porosity (ϕ) in the 2D case might be different from the 3D porosity (ϕ_{3D}).

2.3.2. Geometrical tortuosity

The geometrical tortuosity τ_g, within a porous medium, in a given flow direction y, is calculated through the ratio between the average of the shortest pathway lengths in that direction ($\langle L_{sh,y} \rangle$) by the length of the system domain along the fluid direction (L_y) [57, 58, 17]:

$$\tau_g = \frac{\langle L_{sh,y} \rangle}{L_y} \qquad (5)$$

where $\langle L_{sh,y} \rangle$ is calculated as the average of the shortest pathway lengths calculated as in Section 2.1 for the given flow direction y.

2.3.3. Hydraulic tortuosity

Hydraulic tortuosity was defined by Carman [18] as the ratio of the average length of the fluid paths divided by the length of the sample:

$$\tau_h = \frac{\langle L_h \rangle}{L} \qquad (6)$$

Clennell [20] suggested a kinematical average in which the pathlines are weighted with fluid fluxes; Koponen [9] suggested an approximated form:

$$\langle L_h \rangle \approx \frac{\sum_{i=1}^{N} L_p(r_i) v(r_i)}{\sum_{i=1}^{N} v(r_i)} \qquad (7)$$

where N is a fixed number of streamlines, $L_p(r_i)$ is the path length of the i-th streamline and $v(r_i)$ is the averaged tangential velocity of the fluid at the starting point of the i-th streamline. Koponen et al. [9] suggested also to estimate tortuosity in a fixed direction y from the velocity field simulated with a CFD numerical simulator as:

$$\tau_h = \frac{\langle |v| \rangle}{\langle v_y \rangle} \qquad (8)$$

where $|v|$ is the absolute value of the local flow velocity, v_y is the y component of that velocity and $\langle \rangle$ denotes the spatial average over the pore space. We made use of a numerical simulator based on the Lattice Boltzmann Method (LBM) to simulate the fluid flow in the porous media at the pore-scale and obtain the velocity field and calculate the hydraulic tortuosity (τ_h) with Eq. 8.

7

We also verified the invariance of calculated tortuosity with respect to the variation of the applied pressure gradient until laminar flow conditions are guaranteed ($Re \leq 2$) [59], where the Reynolds number R_e was calculated as [26]:

$$Re = \frac{\rho v d_c}{\mu} \tag{9}$$

where d_c is the characteristic length scale, ρ and μ are the density and the dynamic viscosity of the fluid respectively. There is not just one way to define the characteristic length in a porous medium, sometimes it is equal to the grain diameter [26], others it involves the hydraulic radius (or hydraulic diameter)[60, 61, 62]. We adopted the image-based definition introduced by [63] and later proposed by [64]:

$$d_c = \pi \frac{V_b}{S_w} = \pi \frac{r_H}{\phi} \tag{10}$$

where V_b is the total volume of the bulk system (pore and grain) and S_w is the wetted surface (surface area between grain and void). Eq. 10 represents a sort of average grain size diameter.

2.3.4. Effective porosity

For low porosity materials, a large part of the total pore space may be nonconducting [9]. The effective porosity ϕ_e is defined as the percentage of interconnected conductive pore space with respect to the bulk volume [21]. We proposed a purely geometrical calculation, based on path-finding:

$$\phi_e = \frac{N_{pp}}{N_{px}} \tag{11}$$

where N_{pp} is the number of image pixels belonging to the portion of pore channels crossed by a pathway (in X or Y direction) and N_{px} the total number of image pixels. To this end, for each pathway, all pixels comprised in the pore section orthogonal to the local path direction were considered (see Fig. 1).

For comparison, the effective porosity can be calculated from a rock image by flow simulation [9]:

$$\phi_e = \frac{N_s}{N_l} \tag{12}$$

where, according to [9], N_s is the number of grid cells crossed by streamlines and N_l is the total number of grid cells. To reduce the computational effort, we calculated the effective porosity by applying a cutoff on the local velocity $|v|$ obtained by numerical simulations. Preliminary analysis on the velocity field distribution showed that the velocities of one order of magnitude lower than average value were not significantly contributing to the flow. Based on that velocity threshold was fixed. For each sample, two simulations were performed: the first with imposing pressure gradient in the X direction and the second with imposing pressure gradient in the Y direction. Effective porosity was then calculated merging the identified cells contributing to the flow in both the X

8

and Y cases.

In addiction, the connected porosity (ϕ_c), i.e. the fraction of pore space actually connected, is also obtainable from the hydraulic simulation. In fact, the isolated pore space is not affected by the imposed pressure difference and remains at the initial pressure condition ($p = p_i$), giving:

$$\phi_c = \phi - \frac{N_{pi}}{N_l} \tag{13}$$

where N_{pi} is the number of porous grid cells with $p = p_i$ and N_l is the total number of grid cells. ϕ_c represents a first estimate of the pore fraction that can be potentially involved in the fluid flow. By definition, $\phi_e \leq \phi_c$.

3. Preliminary validation on elementary cases

As a preliminary validation step, three simple cases were analyzed: a thin curved channel (Case 1), a thick curved channel (Case 2) and a slanted straight channel, inclined of 23° (Case 3); details are given in Table 1. In these cases, the hydraulic radius coincides with the radius of the capillary tube, the effective porosity coincides with the porosity and the tortuosity is easily calculated as the length of the tube median line divided by the extension in the X direction; in particular, for Case 3 $\tau = 1/cos(23°) = 1.086$. The numerical parametrization of the three simple cases is reported in Table 2. The fluid used for the numerical simulation has the following properties: viscosity 0.5 cP, density 1050 kg/m^3. A pressure gradient of 100 Pa/m was applied between inlet and outlet. Laminar flow occurs in all the three cases (Re ≤ 2).

The identified geometrical and hydraulic paths are compared in Fig. 2a, 2b and 2c, respectively. Results are summarized in Table 3.

The pore radius estimated by application of the path-finding algorithm ($\tilde{r}_p$) is in good agreement with the hydraulic radius (r_H), which matches the actual channel radius (r). The estimated tortuosity calculated both with the path-finding approach (τ_g) and the flow simulation (τ_h) are comparable with the theoretical values (τ). In more detail, τ_h and τ_g give an excellent estimate of tortuosity in Case 3. In the presence of curves (i.e. Case 1 and Case 2), the computed geometrical tortuosity (τ_g) is smaller than the hydraulic tortuosity (τ_h) because the shortest path is a slanted line crossing out the bight, while the hydraulic path follows the tube curvature; the discrepancy is more significant when pore radius is larger (Case 2). Notice that in Case 1 the hydraulic path follows the channel median line, while in Case 2 the hydraulic path does not perfectly follow the channel median line; as a consequence, in Case 2 the computed hydraulic tortuosity differs a little from the analytic value.

As expected, effective porosity estimated by the path-finding algorithm (ϕ_{eg}) matches the total porosity. Effective porosity estimated by flow simulation (ϕ_{eh}) is slightly lower, due to the combination of no-slip effect at the solid-fluid interface, numerical discretization and velocity field processing.

Table 1: Validation cases.

	Image dimensions (px × px)	Resolution (ppcm)	ϕ (-)	τ (-)	r (mm)
Case 1	793 × 623	4170	0.061	1.571	0.030
Case 2	745 × 736	3920	0.360	1.512	0.223
Case 3	491 × 298	2650	0.206	1.086	0.108

Table 2: Parameters for the numerical simulation of validation cases.

	n_x (l.u.)	n_y (l.u.)	Δx (μm/l.u.)	Re (-)
Case 1	793	623	2.4	0.0046
Case 2	745	736	2.55	1.97
Case 3	491	298	3.77	0.3443

4. Case studies: 2D images of sedimentary rocks

The geometrical and hydrodynamic characterization is carried out on a set of images obtained from thin sections of 3D samples of sedimentary rocks. In this study we analyzed two medium-to-fine-grained sandstone and a oolite: Berea sand ($D_{50} = 23\mu m$ [65]), Hostun sand ($D_{50} = 300\mu m$ [66]) and Caicos ooid ($D_{50} = 420\mu m$ [67]). The three rocks are characterized by very different pore geometry. Berea sand is characterized by high difference between pore throat and pore body dimension. Hostun sand is relatively homogeneous, characterized by well-sorted predominantly quartz angular grains [68]. Caicos ooid is relatively homogeneous and characterized by round calcite grains [67]. Their high porosity and permeability values make them a potential source of oil and natural gas, therefore they can be used as standard rocks for various applications such as core analysis, flooding experiment, testing the efficiency of chemical surfactants and studying the drainage capacity in granular soil ([69, 70, 71]). Literature images of rock samples were used. When available, multiple samples of the same material were analyzed. For Berea sand a black and white image of a horizontal sample [7] widely used in literature (ex. [72], [16]) was adopted; the image is shown in figure 3a and named in the following as case BE30. For Hostun sand, X-ray micro-tomography images of horizontal sections of three different samples were considered: a section with $\phi = 49\%$ ([73]), named in the following case HO49; a small horizontal section with $\phi = 56\%$ ([74]), named in the following case HO56; a more extended section with $\phi = 47\%$ ([74]), named in the following as case HO47. For Caicos ooid, X-ray micro-tomography of two samples were available: a small horizontal section ([74]), named in the following CA52, and a more extended vertical section, already segmented ([67]), named in the following CA42. The grayscale X-ray micro-tomography images were binarized in order to distinguish the solid part from the voids for the following geometrical analysis and hydrodynamic simulation: 1 was assigned to the grain while 0 to the porous domain. To this end, a threshold was applied to the grayscale images based on the histogram of pixels values ([74]). The obtained binarized images are shown in figure 3b-3f and the corresponding parameteri-

10

Table 3: Comparison of parameter estimates obtained by different approaches, geometrical (g) and hydraulic (h), for the validation cases.

	r_H (mm)	$\tilde{r}_p$ (mm)	τ_g $(-)$	$\tau_h(-)$	ϕ_{eg} $(-)$	ϕ_{eh} $(-)$
Case 1	0.030	0.029	1.530	1.571	0.061	0.057
Case 2	0.231	0.221	1.268	1.486	0.359	0.353
Case 3	0.110	0.115	1.087	1.083	0.206	0.198

zation is reported in table 4, where the 2D porosity values were calculated from images.

In order to observe hydrodynamic behavior, the smallest pore size should be 4-5 lattice units [75]. When the pixel resolution of the rock images did not satisfy the condition above, we re-sized figures by bi-cubic interpolation, imposing a number of lattices that guarantees at least 5 lattices in the smallest pore channels.The numerical parametrization of the considered case studies is reported in Table 5. The fluid used for the numerical simulation has the following properties: viscosity 0.5 cP, density 1050 kg/m^3. A pressure gradient of 100 Pa/m was applied between inlet and outlet. Laminar flow occurs in all the three cases (Re $\leq$ 2). Case studies were analyzed separately in the X and Y directions, to assess eventual discrepancy in tortuosity which could be an indicator of permeability anisotropy.

Table 4: Case studies:images details.

	Image dimensions (px $\times$ px)	Resolution (ppcm)	ϕ (-)
BE30	769 $\times$ 624	4120	0.3
HO49	640 $\times$ 640	1450	0.49
HO56	449 $\times$ 549	1915	0.56
HO47	657 $\times$ 654	858	0.47
CA52	546 $\times$ 549	1414	0.52
CA42	448 $\times$ 417	531	0.42

5. Results

Results of the geometrical approach proposed for the estimation of tortuosity and effective porosity are summarized in Table 6 and compared with hydraulic approach results, including the connected porosity. In addition, the mode of pore radius (r_p) estimated through path finding approach is compared with the calculated hydraulic radius (r_H). We point out that in CA42 there is no connectivity along the X direction, thus it was not possible to estimate the tortuosity in X direction (τ_x) for this case. We reported graphical results for BE30 (see Figs. 4- 6), and for most interesting comparing cases. Graphical results comprehend: geometrical v.s. hydraulic paths (ex. Fig.4); comparison of effective porosity map obtained with the two approaches (ex. Fig.5); pore radius analysis conducted by the proposed path-finding approach (overall pore radius distribution

and pore radius evolution along a single path, ex. Fig. 6b).

In all cases, tortuosity values calculated with the two methods are comparable (discrepancy less than 10%) and the geometrical tortuosity is slightly smaller than the hydraulic tortuosity, as expected [20, 17]. The only exception is HO47, which shows a discrepancy of around 16%; this is due to local significant narrowing of the pore radius along the shortest paths which induces the hydraulic flux favor alternative ways even if longer (Fig. 11). Comparing our results with literature, Berea tortuosity results are coherent with the gamma-shaped distribution with minimum value 1.07 and most probable value near to 2, reported in [29] and just below the range 1.6-2.8 reported in [76]. The values of tortuosity summarized in Table 6 were compared with the geometrical tortuosity calculated adopting the model proposed by Ghanbarian et al. [33] and based on percolation theory and finite-size scaling approach. Imposing a fractal dimension equal to 1.13, tortuosity values calculated by the Ghanbarian model are: $\tau_g = 1.24$ for Berea and $\tau_g = 1.16$ for Hostun when ϕ_{eg} is adopted; $\tau_h = 1.26$ for Berea and $\tau_h = 1.17$ when ϕ_{eh} is adopted.

The pore radius distribution obtained by path finding algorithm appears to be reliable. For Berea scenario, for instance, the distribution (Fig. 6a) is in good agreement with the literature: 31% of pore throats diameter about 10 μm[77]; 5 μm as the most frequent pore throat radius [54]; 37% of relative pore volume characterized by 7-10 μm of pore radius [78]. Hostun results are comparable with the pore diameter distribution calculated with Mercury Intrusion Porosity, and analysis of Scanning Electron Microscopy images [66], which shows a mode around 60-90 μm. Reasonable agreement (order of magnitude) is observed between the hydraulic radius and the mode of pore radius distribution obtained by the path-finding approach in all scenarios (Tab. 6), thus suggesting that hydraulic radius formula (Eq. 4) is reasonably representative of the effective pore radius of the sample, at least if the pore radius variations are limited; the representativeness of r_H is poorer when the pore radii is highly variable (ex. BE30, HO47, CA42).

In all the cases except CA42 the connected porosity approaches the total porosity ($\phi_{ch} \approx \phi$). Conversely, CA42 shows a very poor connection ($\phi_{ch} << \phi$), limited to Y direction (Fig. 9). By way of example, fig. 7 shows the difference in connected porosity between HO49 and CA42 which both shows an effective porosity significantly lower than the total porosity. Good agreement is observed in terms of estimated effective porosity in all scenarios (Tab. 6). Small sections (CA57 and HO56), characterized by higher porosities, are almost completely fluxed (i.e. $\phi - \phi_e < 10\%$). Conversely, in HO49, HO47 and CA42 significant dead zones ($\phi - \phi_e \approx 30\%$ or greater) are clearly identified by both approaches (ex. Fig. 8). Discrepancies between effective porosity estimated with the two approaches (geometrical vs hydraulic) is below 5% in most cases. These differences are due to the different treatment of meandering zones by the geometrical and hydraulic method, as clear in Fig. 8. Trajectories identified by the path-finding algorithm agree with the paths shown by the velocity map in HO49 (Fig. 10), H56, CA52 and CA42, and, as consequence, the identified dead zones are well comparable (ex. Fig.8 and Fig.9). On the contrary, in BE30 (Fig.4 , Fig.5)

12

and HO47, the more complex pore structure, characterized by multiple possible paths between the entry and outlet points, and the higher variability in the pore radius induce local discrepancies between the geometrical and hydraulic path: the fluid flow, in presence of a conspicuous narrowing of the pore radius, choose to follow a wider pathway, even if longer (Fig. 11).

Table 5: Parameters for the numerical simulation of the analyzed case studies.

	n_x (l.u.)	n_y (l.u.)	Δx ($\mu m/l.u.$)	Re (-)
BE30	1706	1367	1.04	3.18E-04
HO49	1200	1200	3.45	0.054
HO56	1000	1209	2.5	0.0192
HO47	1200	1038	6.66	0.0281
CA52	800	804	5	0.0526
CA42	1200	1121	7.5	0.006

Table 6: Comparison of parameter estimates obtained by different approaches, geometrical (g) and hydraulic (h), for the analyzed case studies.

	r_H (μm)	$\tilde{r}_p$ (μm)	τ_{xg} (-)	τ_{xh} (-)	τ_{yg} (-)	τ_{yh} (-)	ϕ_{eg} (-)	ϕ_{eh} (-)	ϕ_{ch} (-)
BE30	14.6	7.29	1.250	1.416	1.437	1.542	0.277	0.256	0.3
HO49	71.7	58.6	1.269	1.459	1.243	1.357	0.374	0.362	0.481
HO56	52.6	57.5	1.153	1.322	1.14	1.362	0.533	0.506	0.559
HO47	69.5	47.2	1.257	1.641	1.22	1.6	0.342	0.355	0.459
CA52	61.4	38.9	1.128	1.301	1.118	1.278	0.508	0.489	0.519
CA42	78.8	95.4	-	-	1.317	1.65	0.065	0.056	0.31

6. Conclusions

In the current paper we explore the possibility of adopting a geometrical analysis based on path-finding algorithm for characterization of pore network geometry and connectivity of 2D binary images of rock samples representative of real geological formations. In order to validate the results provided by geometrical analysis we implemented and applied a LBM hydrodynamic numerical simulator and compared the results. The differences between results provided by the two approaches were more evident in scenarios characterized by the presence of large pores (i.e. Case 2), or high variability of pore radius along pathways and multiple available pathways (i.e. Berea B30 and Hostun HO47).In fact, the geometrical approach always selects the shortest way, without accounting for realistic fluid ways or pore radius thickness, even in the presence of extremely narrow pores.

Results showed that even if hydrodynamic simulation was more accurate in reproducing the flow behavior, the path-finding approach could give reasonable estimates of tortuosity and could also be successfully applied for analyzing the

distribution of effective pore radius, as well as for estimating the effective porosity without the use of a time consuming simulator.

In future work, the algorithm for effective pore volume identification via pathfinding could be developed to exclude meandering zones, thus further improving the estimate.

References

[1] A. Anbari, H.-T. Chien, S. S. Datta, W. Deng, D. A. Weitz, J. Fan, Microfluidic model porous media: fabrication and applications, Small 14 (18) (2018) 1703575.

[2] M. J. Blunt, Flow in porous media—pore-network models and multiphase flow, Current opinion in colloid & interface science 6 (3) (2001) 197–207.

[3] M. Venturoli, E. S. Boek, Two-dimensional lattice-boltzmann simulations of single phase flow in a pseudo two-dimensional micromodel, Physica A: Statistical Mechanics and its Applications 362 (1) (2006) 23–29.

[4] G. Viggiani, S. A. Hall, R. E., ALERT Doctoral School 2012. Advanced experimental techniques in geomechanics., The Alliance of Laboratories in Europe for Research and Technology, 2012.

[5] M. Wu, F. Xiao, R. M. Johnson-Paben, S. T. Retterer, X. Yin, K. B. Neeves, Single-and two-phase flow in microfluidic porous media analogs based on voronoi tessellation., Lab on a Chip 12 (2) (2012) 253–261.

[6] A. Laleian, A. J. Valocchi, C. J. Werth, An incompressible, depth-averaged lattice boltzmann method for liquid flow in microfluidic devices with variable aperture., Computation 3 (4) (2015) 600–615.

[7] E. S. Boek, M. Venturoli, Lattice-boltzmann studies of fluid flow in porous media with realistic rock geometries, Computers and Mathematics with Applications 59 (7) (2010) 2305 – 2314. `doi:https://doi.org/10.1016/j.camwa.2009.08.063`.

[8] A. Koponen, M. Kataja, J. Timonen, Permeability and effective porosity of porous media, Physical Review E 56 (3) (1997) 3319. `doi:https://doi.org/10.1103/PhysRevE.56.3319`.

[9] A. Koponen, M. Kataja, J. Timonen, Tortuous flow in porous media, Physical review E 54 (1996) 406–410. `doi:10.1103/PhysRevE.54.406`.

[10] A. Ghassemi, A. Pak, Pore scale study of permeability and tortuosity for flow through particulate media using lattice boltzmann method., International Journal for Numerical and Analytical Methods in Geomechanics 35 (8) (2011) 886–901.

[11] Z. Li, S. Galindo-Torres, G. Yan, A. Scheuermann, L. Li, A lattice boltzmann investigation of steady-state fluid distribution, capillary pressure and relative permeability of a porous medium: Effects of fluid and geometrical properties, Advances in water resources 116 (2018) 153–166.

[12] P. Yang, Z. Wen, R. Dou, X. Liu, Permeability in multi-sized structures of random packed porous media using three-dimensional lattice boltzmann method., International Journal of Heat and Mass Transfer 106 (2017) 1368–1375.

[13] C. Pan, L. Luo, C. Miller, An evaluation of lattice boltzmann schemes for porous medium flow simulation, Computers & Fluids - COMPUT FLUIDS 35 (2006). `doi:10.1016/j.compfluid.2005.03.008`.

[14] A. Eshghinejadfard, L. Daroczy, G. Janiga, D. Thevenin, Calculation of the permeability in porous media using the lattice boltzmann method, International Journal of Heat and Fluid Flow 62 (2016) 93–103.

[15] B. Ferreol, D. H. Rothman, Lattice-boltzmann simulations of flow through fontainebleau sandstone., In Multiphase flow in porous media (1995) 3–20.

[16] M. Xu, H. Liu, Prediction of immiscible two-phase flow properties in a two-dimensional berea sandstone using the pore-scale lattice boltzmann simulation, Eur. Phys. J. 41 (124) (2018). `doi:https://doi.org/10.1140/epje/i2018-11735-3`.

[17] B. Ghanbarian, A. G. Hunt, R. P. Ewing, M. Sahimi, Tortuosity in porous media: a critical review, Soil science society of America journal 77 (5) (2013) 1461–1477.

[18] P. C. Carman, Fluid flow through granular beds, Trans. Inst. Chem. Eng. 15 (1937) 150–166.

[19] P. Adler, Porous media: geometry and transports, Elsevier, 2013.

[20] M. Clennell, Tortuosity: A guide through the maze, Geological Society, London, Special Publications 122 (1997) 299–344. `doi:10.1144/GSL.SP.1997.122.01.18`.

[21] T. Ahmed, Reservoir Engineering Handbook, Elsevier, 2010.

[22] F. A. Dullien, Porous media: fluid transport and pore structure, Academic press, 2012.

[23] A. E. Scheidegger, The Physics of Flow Through Porous Media (3rd Edition), University of Toronto Press, 1974.

[24] M. Wyllie, M. Spangler, Application of electrical resistivity measurements to problem of fluid flow in porous media, AAPG Bulletin 36 (2) (1952) 359–403.

[25] A. T. Corey, et al., Mechanics of heterogeneous fluids in porous media., Water Resources Publications., 1977.

[26] J. Bear, Dynamics of fluids in porous media, Courier Corporation, 2013.

[27] A. Rabbani, S. Ayatollahi, Comparing three image processing algorithms to estimate the grain-size distribution of porous rocks from binary 2d images and sensitivity analysis of the grain overlapping degree, Special Topics and Reviews in Porous Media 6 (2015) 71–89. `doi:10.1615/ SpecialTopicsRevPorousMedia.v6.i1.60`.

[28] P. A. Lock, X. Jing, R. W. Zimmerman, E. M. Schlueter, Predicting the permeability of sandstone from image analysis of pore structure., Journal of applied physics 92 (10) (2002) 6311–6319.

[29] W. B. Lindquist, S. M. Lee, D. A. Coker, K. W. Jones, P. Spanne, Medial axis analysis of void structure in three-dimensional tomographic images of porous media, Journal of Geophysical Research 101 (B4) (1996) 8297–8310.

[30] W. C. Sun, J. E. Andrade, J. W. Rudnicki, Multiscale method for characterization of porous microstructures and their impact on macroscopic effective permeability., International Journal for Numerical Methods in Engineering 88 (12) (2011) 1260–1279.

[31] Y. Ju, P. Liu, D. Zhang, J. Dong, P. Ranjith, C. Chang, Prediction of preferential fluid flow in porous structures based on topological network models: Algorithm and experimental validation, Science China Technological Sciences 61 (8) (2018) 1217–1227.

[32] L. M. Keller, L. Holzer, R. Wepf, P. Gasser, 3d geometry and topology of pore pathways in opalinus clay: Implications for mass transport, Applied Clay Science 52 (1-2) (2011) 85–95.

[33] B. Ghanbarian, A. G. Hunt, M. Sahimi, R. P. Ewing, T. E. Skinner, Percolation theory generates a physically based description of tortuosity in saturated and unsaturated porous media, Soil Science Society of America Journal 77 (6) (2013) 1920–1929.

[34] A. G. Hunt, M. Sahimi, Flow, transport, and reaction in porous media: Percolation scaling, critical-path analysis, and effective medium approximation, Reviews of Geophysics 55 (4) (2017) 993–1078.

[35] R. I. Al-Raoush, I. T. Madhoun, Tort3d: A matlab code to compute geometric tortuosity from 3d images of unconsolidated porous media., Powder technology 320 (2017) 99–107.

[36] I. Vlahinic, E. Andò, G. Viggiani, J. Andrade, Towards a more accurate characterization of granular media: Extracting quantitative descriptors from tomographic images, Granular Matter 16 (02 2014). `doi: 10.1007/s10035-013-0460-6`.

16

[37] M. A. Hashemi, G. Khaddour, B. François, T. J. Massart, S. Salager, A tomographic imagery segmentation methodology for three-phase geomaterials based on simultaneous region growing, Acta Geotechnica 9 (5) (2014) 831–846. `doi:10.1007/s11440-013-0289-5`.

[38] D. Saladra, M. Kopernik, Qualitative and quantitative interpretation of sem image using digital image processing, Journal of Microscopy 264 (1) (2016) 102–124. `doi:10.1111/jmi.12431`.

[39] P. E. Hart, N. J. Nilsson, B. Raphael, A formal basis for the heuristic determination of minimum cost paths, IEEE transactions on Systems Science and Cybernetics 4 (2) (1968) 100–107.

[40] N. J. Nilsson, Principles of artificial intelligence, Tioga Pub. Co., Palo Alto, CA, 1980.

[41] N. J. Nilsson, Principles of artificial intelligence, Morgan Kaufmann, 2014.

[42] G. R. McNamara, G. Zanetti, Use of the boltzmann equation to simulate lattice gas automata, Physical review letters 61 (20) (1988) 2332–2335. `doi:10.1103/physrevlett.61.2332`.

[43] T. Krüger, H. Kusumaatmaja, A. Kuzmin, O. Shardt, G. Silva, E. M. Viggen, The Lattice Boltzmann Method - Principles and Practice, Springer, 2017. `doi:10.1007/978-3-319-44649-3`.

[44] R. Benzi, S. Succi, M. Vergassola, The lattice boltzmann equation: theory and applications, Physics Reports 222 (3) (1992) 145 – 197. `doi:https://doi.org/10.1016/0370-1573(92)90090-M`.

[45] S. Chen, G. D. Doolen, Lattice boltzmann method for fluid flows, Annual Review of Fluid Mechanics 30 (1) (1998) 329–364. `doi:10.1146/annurev.fluid.30.1.329`.
URL `https://doi.org/10.1146/annurev.fluid.30.1.329`

[46] Z. Guo, T. Zhao, Lattice boltzmann model for incompressible flows through porous media, Physical review. E, Statistical, nonlinear, and soft matter physics 66 (2002) 036304. `doi:10.1103/PhysRevE.66.036304`.

[47] A. Nabovati, A. Sousa, Fluid flow simulation in random porous media at pore level using lattice boltzmann method, Journal of Engineering Science and Technology 2 (12 2007). `doi:10.1007/978-3-540-75995-9_172`.

[48] M. Matyka, A. Khalili, Z. Koza, Tortuosity-porosity relation in porous media flow, Physical review E 78 (2008) 026306. `doi:10.1103/PhysRevE.78.026306`.

[49] P. Wang, Lattice boltzmann simulation of permeability and tortuosity for flow through dense porous media, Mathematical Problems in Engineering 2014 (07 2014). `doi:10.1155/2014/694350`.

[50] P. L. Bhatnagar, E. P. Gross, M. Krook, A model for collision processes in gases. i. small amplitude processes in charged and neutral one-component systems, Phys. Rev. 94 (1954) 511–525. `doi:10.1103/PhysRev.94.511`.

[51] Y. H. Qian, D. d'Humieres, P. Lallemand, Lattice BGK models for navier-stokes equation, Europhysics Letters (EPL) 17 (6) (1992) 479–484. `doi:10.1209/0295-5075/17/6/001`.

[52] A. J. C. Ladd, Numerical simulations of particulate suspensions via a discretized boltzmann equation. part 1. theoretical foundation, Journal of Fluid Mechanics 271 (1994) 285–309. `doi:10.1017/S0022112094001771`.

[53] Q. Zou, X. He, On pressure and velocity boundary conditions for the lattice boltzmann bgk model, Physics of Fluids 9 (6) (1997) 1591–1598. `doi:10.1063/1.869307`.

[54] P. E. Øren, S. Bakke, Reconstruction of berea sandstone and pore-scale modelling of wettability effects, Journal of Petroleum Science and Engineering 39 (3-4) (2003) 177–199.

[55] J. Soete, S. Claes, H. Claes, N. Janssens, V. Cnudde, M. Huysmans, R. Swennen, Lattice boltzmann simulations of fluid flow in continental carbonate reservoir rocks and in upscaled rock models generated with multiple-point geostatistics, Geofluids 2017 (2017).

[56] Mathworks, Image Processing Toolbox User's Guide (2017).

[57] R. Dias, J. A. Teixeira, M. Mota, A. Yelshin, Tortuosity variation in a low density binary particulate bed, Separation and Purification Technology 51 (2) (2006) 180–184.

[58] W. Sobieski, S. Lipiński, The analysis of the relations between porosity and tortuosity in granular beds, Technical Sciences/University of Warmia and Mazury in Olsztyn (2017).

[59] M. Aminpour, S. A. Galindo-Torres, A. Scheuermann, L. Li, Pore-scale behavior of darcy flow in static and dynamic porous media, Phys. Rev. Applied 9 (2018) 064025. `doi:10.1103/PhysRevApplied.9.064025`.

[60] S. Ergun, A. A. Orning, Fluid flow through randomly packed columns and fluidized beds, Industrial & Engineering Chemistry 41 (6) (1949) 1179–1184.

[61] S. Ergun, Fluid flow through packed columns, Chem. Eng. Prog. 48 (1952) 89–94.

[62] T. Papathanasiou, B. Markicevic, E. Dendy, A computational evaluation of the ergun and forchheimer equations for fibrous porous media, Physics of Fluids 13 (10) (2001) 2795–2804.

[63] P. Mostaghimi, B. Bijeljic, M. Blunt, et al., Simulation of flow and dispersion on pore-space images, SPE Journal 17 (04) (2012) 1–131.

[64] M. J. Blunt, Multiphase flow in permeable media: A pore-scale perspective, Cambridge University Press, 2017.

[65] Z. Gao, Q.-H. Hu, Investigating the effect of median pore-throat diameter on spontaneous imbibition, Journal of Porous Media 18 (2015) 1231–1238. `doi:10.1615/JPorMedia.v18.i12.60`.

[66] E. Vitorge, S. Szenknect, J. Martins, J.-P. Gaudet, Size and concentration-dependent deposition of fluorescent silica colloids in saturated sand columns: Transport experiments and modeling, Environmental science. Processes and impacts 15 (07 2013). `doi:10.1039/c3em30860j`.

[67] E. Andó, S. A. Hall, G. Viggiani, J. Desrues, P. Bésuelle, Grain-scale experimental investigation of localised deformation in sand: a discrete particle tracking approach, Acta Geotechnica 7 (1) (2012) 1–13. `doi:https://doi.org/10.1007/s11440-011-0151-6`.

[68] P. Churcher, P. French, J. Shaw, L. Schramm, et al., Rock properties of berea sandstone, baker dolomite, and indiana limestone, in: SPE International Symposium on Oilfield Chemistry, Vol. 20, Society of Petroleum Engineers Anaheim, CA, 1991, p. 22.

[69] M. Sato, K. Panaghi, N. Takada, M. Takeda, Effect of bedding planes on the permeability and diffusivity anisotropies of berea sandstone, Transport in Porous Media 127 (3) (2019) 587–603.

[70] K. Y. Kim, L. Zhuang, H. Yang, H. Kim, K.-B. Min, Strength anisotropy of berea sandstone: results of x-ray computed tomography, compression tests, and discrete modeling, Rock Mechanics and Rock Engineering 49 (4) (2016) 1201–1210.

[71] T. Sharma, G. Suresh Kumar, J. S. Sangwai, Enhanced oil recovery using oil-in-water (o/w) emulsion stabilized by nanoparticle, surfactant and polymer in the presence of nacl, Geosystem Engineering 17 (3) (2014) 195–205.

[72] Q. Gu, H. Liu, Y. Zhang, Lattice boltzmann simulation of immiscible two-phase displacement in two-dimensional berea sandstone, Applied Sciences 8 (2018) 1497. `doi:10.3390/app8091497`.

[73] G. Viggiani, P. Bésuelle, S. Hall, J. Desrues, Sand deformation at the grain scale quantified through x-ray imaging, Advances in Computed Tomography for Geomaterials: GeoX 2010 (2010) 1–16.

[74] E. Ando, Experimental investigation of microstructural changes in deforming granular media using x-ray tomography, PhD dissertation, Université de Grenoble (2013).

[75] S. Succi, The Lattice Boltzmann Method for Fluid Dynamics and Beyond, Oxford University Press, 2001.

[76] Geometry of Pore Structure in Pressurized Berea Sandstone., International Society for Rock Mechanics and Rock Engineering, Taylor and Francis Group, 2009.

[77] K. Li, R. Horne, Fractal characterization of the geysers rock, Geothermal Resources Council Transactions 27 (2003).

[78] J. Shi, Z. Xue, S. Durucan, Supercritical co2 core flooding and imbibition in berea sandstone — ct imaging and numerical simulation, Energy Procedia 4 (2011). `doi:https://doi.org/10.1016/j.egypro.2011.02.471`.
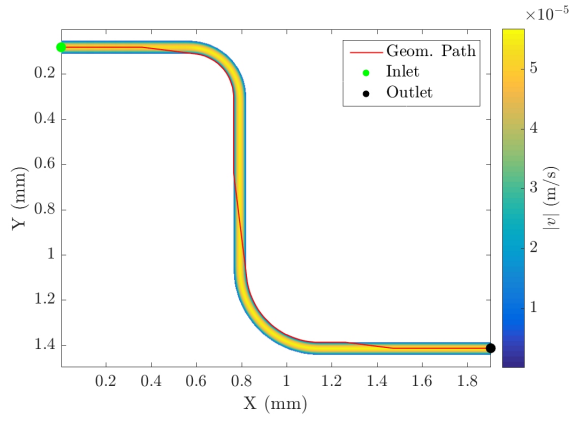
(a)
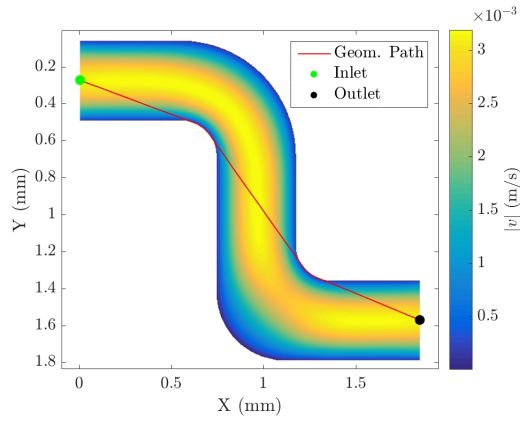
(b)
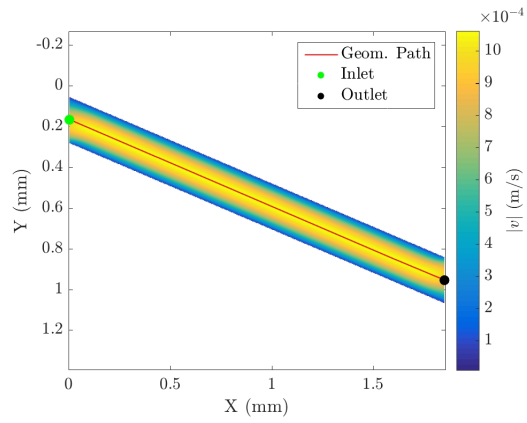
(c)

Figure 2: Simulated velocity map ($|v|$) vs. detected geometrical paths considering flow in the X direction for the validation cases: (a) Case 1, (b) Case 2, (c) Case 3.

(a) BE30

(b) CA52

(c) CA42

(d) HO49

(e) HO56

(f) HO47
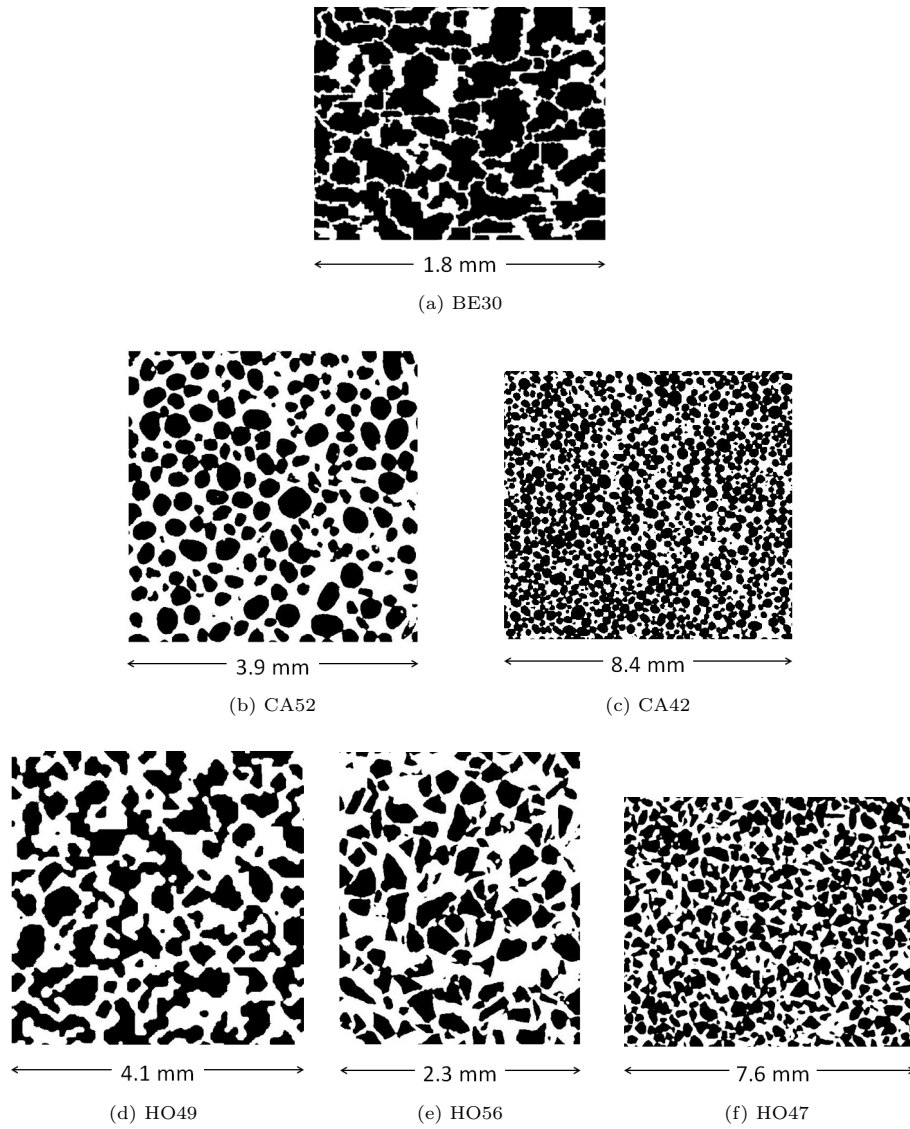
Figure 3: Case studies: 2D images of sedimentary rocks.
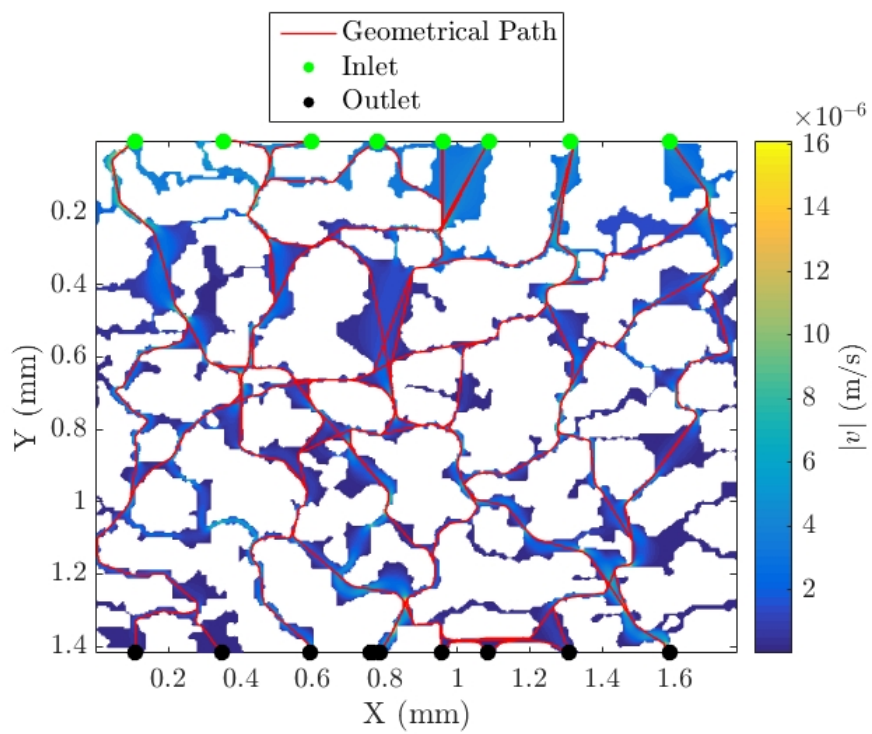
Figure 4: Simulated velocity map ($|v|$) vs. detected geometrical paths considering flow in the Y direction for the Berea scenario.
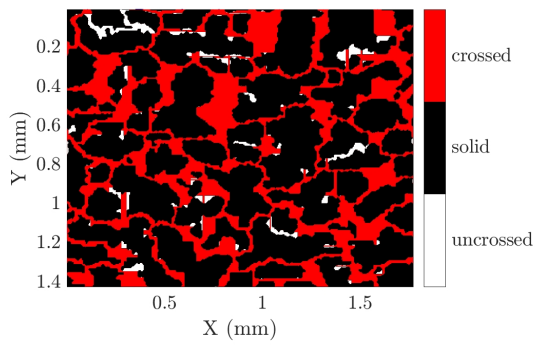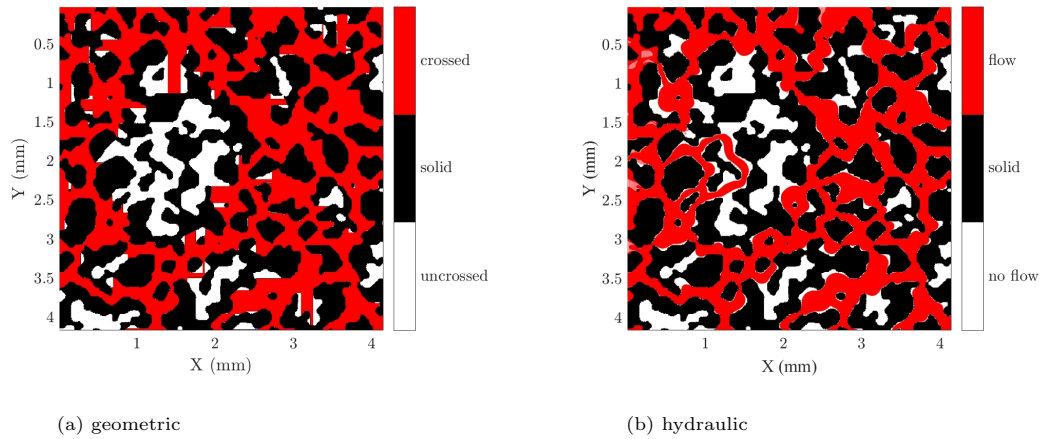
(a) geometric
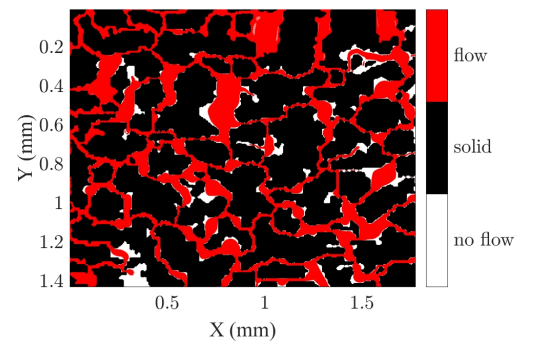
(b) hydraulic

Figure 5: Pore volume interested by flow (red) and dead zones (white), for the Berea scenario, identified by applying (a) the path-finding algorithm vs. (b) a cutoff on simulated velocity.
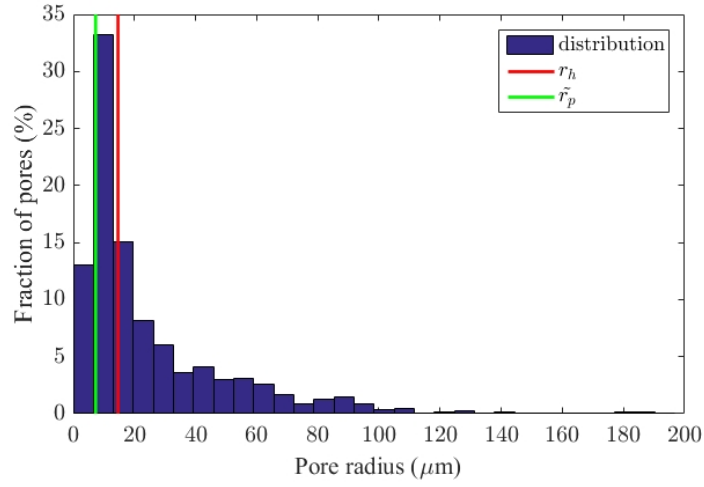
(a)
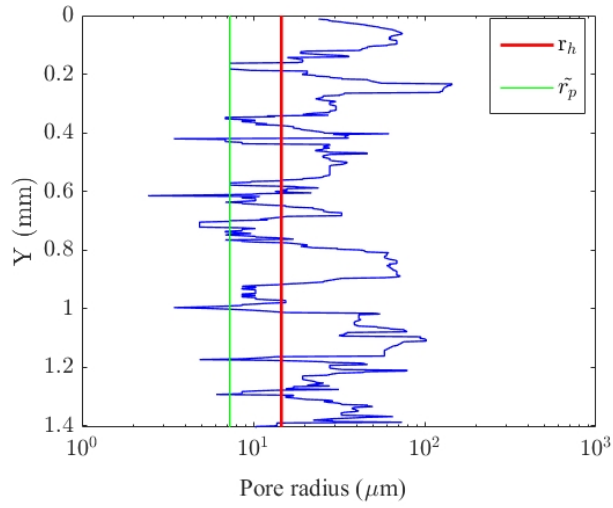
(b)

Figure 6: Pore radius estimation from the path-finding approach for the Berea scenario: (a) pore radius distribution compared with hydraulic radius (red line) ; (b) pore radius variation along a single vertical path, compared with the mode of the pore radius along the selected path (green line) and the hydraulic radius (red line).

(a) HO49

(b) CA42
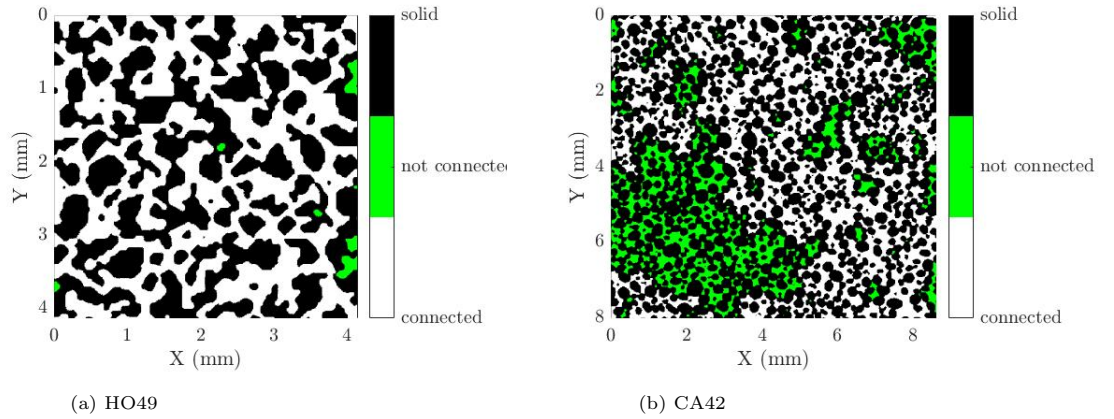
Figure 7: Connected pore volume (white) and isolated zones (green), for the Hostun scenario HO49 (a) and CA42 scenario (b)

(a) geometric

(b) hydraulic

Figure 8: Pore volume interested by flow (red) and dead zones (white), for the Hostun scenario HO47, identified by applying (a) the path-finding algorithm vs. (b) a cutoff on simulated velocity.
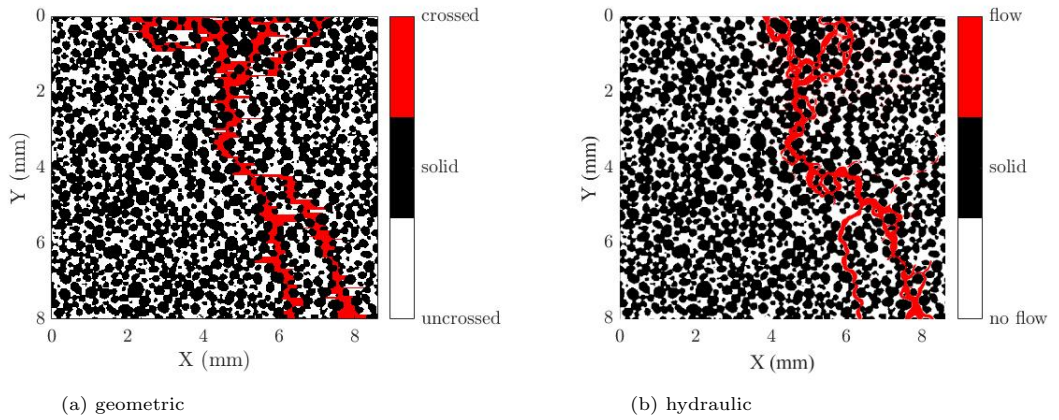
26

(a) geometric

(b) hydraulic

Figure 9: Pore volume interested by flow (red) and dead zones (white), for the Caicos ooid scenario CA42, identified by applying (a) the path-finding algorithm vs. (b) a cutoff on simulated velocity.
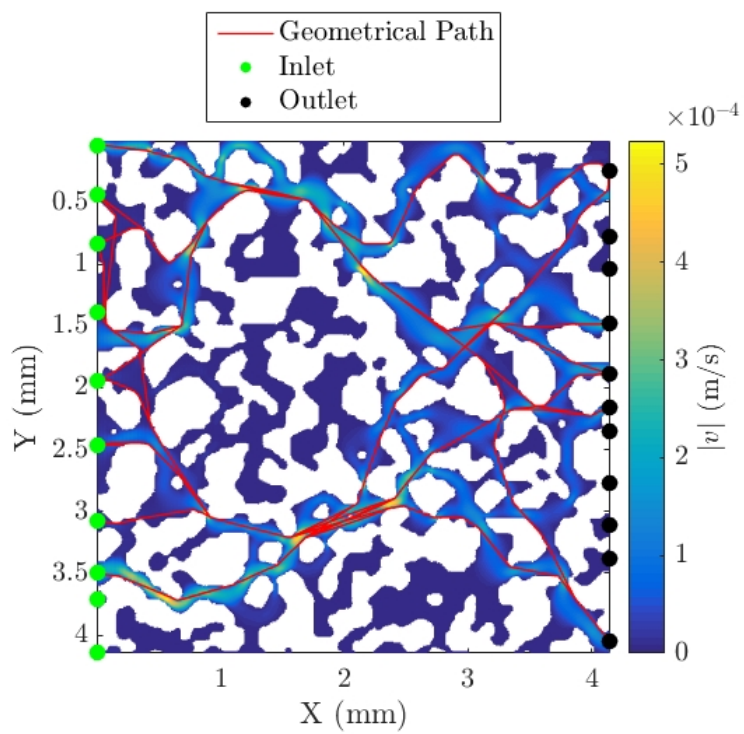
Figure 10: Simulated velocity map ($|v|$) vs. detected geometrical paths considering flow in the X direction for the Hostun scenario.
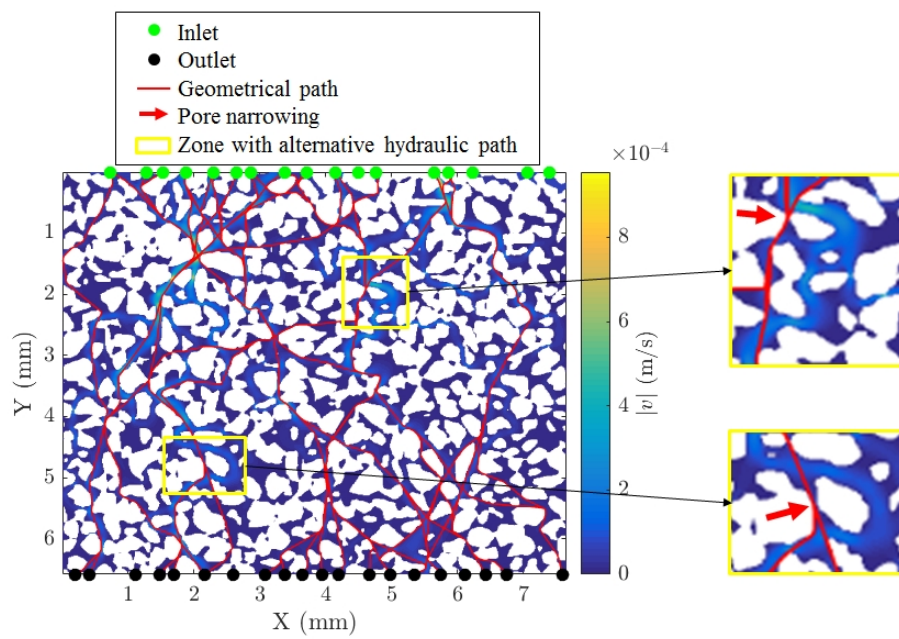
Figure 11: Simulated velocity map ($|v|$) vs. detected geometrical paths considering flow in Y directions for HO47 scenario; pore narrowing imposing a change of hydraulic path with respect to the shortest geometrical path is underlined by red arrows and yellow circles.